SSR manuscript No.
(will be inserted by the editor)

The MASCOT Radiometer MARA for the Hayabusa 2 Mission

M. Grott · J. Knollenberg · B. Borgs · F. Hänschke · E. Kessler · J. Helbert · A. Maturilli · N. Müller

Received: date / Accepted: date

M. Grott
Institute of Planetary Research, German Aerospace Center,
Rutherfordstr. 2, 12489 Berlin, Germany
Tel.: +49-30-67055 419
E-mail: matthias.grott@dlr.de

J. Knollenberg
Institute of Planetary Research, German Aerospace Center,
Rutherfordstr. 2, 12489 Berlin, Germany

B. Borgs
Institute of Planetary Research, German Aerospace Center,
Rutherfordstr. 2, 12489 Berlin, Germany

F. Hänschke
Institute of Photonic Technology,
Albert-Einstein-Straße 9, 07745 Jena, Germany

E. Kessler
Institute of Photonic Technology,
Albert-Einstein-Straße 9, 07745 Jena, Germany

J. Helbert
Institute of Planetary Research, German Aerospace Center,
Rutherfordstr. 2, 12489 Berlin, Germany

A. Maturilli
Institute of Planetary Research, German Aerospace Center,
Rutherfordstr. 2, 12489 Berlin, Germany

N. Müller
Institute of Planetary Research, German Aerospace Center,
Rutherfordstr. 2, 12489 Berlin, Germany

Abstract The MASCOT radiometer MARA is a multi-spectral instrument which measures net radiative flux in six wavelength bands. MARA uses thermopile sensors as sensing elements, and the net flux between the instrument and the surface in the 18° field of view is determined by evaluating the thermoelectric potential between the sensors' absorbing surface and the thermopile's cold-junction. MARA houses 4 bandpass channels in the spectral range of 5.5-7, 8-9.5, 9.5-11.5, and 13.5-15.5 µm, as well as one long-pass channel, which is sensitive in the > 3 µm range. In addition, one channel is similar to that used by the Hayabusa 2 orbiter thermal mapper, which uses a wavelength range of 8-12 µm. The primary science objective of the MARA instrument it the determination of the target asteroid's surface brightness temperature, from which surface thermal inertia can be derived. In addition, the spectral bandpass channels will be used to estimate the spectral slope of the surface in the thermal infrared wavelength range. The instrument has been calibrated using a cavity blackbody, and the temperature uncertainty is 1 K in the long pass channel for target temperatures of > 173 K. Measurement uncertainty in the spectral bandpasses is 1 K for target temperatures above 273 K.

Keywords Hayabusa 2 · MASCOT · Radiometer · Temperature Measurement · Thermal Inertia

1 Introduction

Surface processes on airless solar system bodies are driven by their surface energy balance, which itself is a function of insolation and the thermophysical properties of the surface and shallow subsurface. In addition to being an important parameter for engineering purposes and the thermal design of spacecraft and landers, a small body's surface temperature can influence its spin state as well as its orbit through the Yarkovksy (Rubincam 1995; Chesley et al. 2003; Bottke et al. 2006) and YORB (Paddack 1969; Bottke et al. 2006) effects. The received and emitted radiative fluxes are thus fundamental quantities, which are intimately linked to the surface albedo, emissivity, as well as the surface thermal inertia. While insolation is driven by the reception of solar radiation in the visible wavelength band, re-radiation primarily occurs in the thermal infrared, and knowledge of the relevant fluxes enables studies of the surface thermophysical properties. On this account, radiometers to measure surface brightness temperatures have been payloads on many landed missions including the Mars Science Laboratory (MSL) (Gómez-Elvira et al. 2012) and the Rosetta Philae lander (Spohn et al. 2007, 2015; Biele and Ulamec 2008).

The Mobile Asteroid Surface Scout (MASCOT) (Lange et al. 2012) is part of the Hayabusa 2 mission which will investigate the C-type near earth asteroid (NEA) 1999 JU3 in 2018 and return samples to Earth in 2020. MASCOT will be deployed from the main spacecraft following an initial phase of remote asteroid characterization in 2018, and will then operate for approximately 16 h on primary batteries, covering two day-night cycles of asteroid observation. The lander is equipped with a hopping mechanism, and will in-situ investigate 1999 JU3 at multiple surface sites using its four science instruments, which comprise a near infrared spectrometer (Bibring et al. 2015), a camera (Jaumann et al. 2015), a magnetometer (Herzig et al. 2015), as well as the MAscot RAdiometer (MARA). With resolutions of mm to cm, MASCOT measurements will thereby bridge the gap in length scales between global characterization

from the Hayabusa home position in the sub-solar point, which will achieve a resolution in the 10-100 m range, to the detailed analysis of returned samples on the μm scale. Furthermore, data obtained by the MASCOT instruments will act as ground truth for orbiter measurements and characterize the undisturbed surface before samples have been collected.

In this paper, we will describe the science objectives, design, and calibration of the MARA instrument. MARA design heavily relies on heritage from the Thermal Mapper of the Multi Purpose Sensor (MUPUS-TM, Spohn et al. (2007)) on-board the Rosetta Lander Philae, as well as heritage from the MErcury Radiometer and Thermal Infrared Spectrometer (MERTIS, Arnold et al. (2008); Hiesinger et al. (2010)) for the Bepi-Colombo orbiter. The MARA sensor design is similar to that of the MUPUS-TM, and similar sensors have since been used on the Mars Science Laboratory Ground Temperature Sensor as part of the Rover's Environmental Monitoring Station (GTS-REMS, Gómez-Elvira et al. (2012)). Furthermore, MARA's low noise electronics is direct heritage from MERTIS, thus enabling the development, testing, and successful delivery of the instrument within just over two years.

2 Instrument Design

2.1 Science Objectives

The target asteroid 1999 JU3 is classified as a Cg - type (Bus and Binzel 2002) based on its 0.36-0.92 µm spectrum acquired in 1999 at the Palomar Mountain Observatory (Binzel et al. 2001). The Cg subclass is characterized by stronger UV absorption short of 0.55 µm and a relatively flat spectrum between 0.55-0.85 µm (Bus and Binzel 2002). Additional spectra of 1999 JU3 were acquired at the Multi Mirror Telescope (MMT) in 2007 (Vilas 2008), and the median of these spectra is also flat between 0.55-0.85 µm. However one spectrum shows an absorption feature at 0.7 µm, which is typical of the Ch and Cgh subclasses. This could indicate the presence of hydrous alteration (thus the h in Ch) for C-type main belt asteroids (Bus and Binzel 2002). The 0.7 µm absorption feature matches a feature of antigorite, an iron rich phyllosilicate that forms by hydrous alteration of olivine, and it has been proposed that the apparent variation of the spectrum in time indicates a versatile surface composition (Vilas 2008). However, more recent observations have not confirmed the 0.7 µm absorption feature (Lazzaro et al. 2013), and rather indicate that 1999 JU3 has featureless spectra with very little variation, an observation supported by the results of Abe et al. (2008).

1999 JU3 has a low visual geometric albedo, compatible with a C-type taxonomic-type classification. Values between $p_V = 0.070 \pm 0.006$ (Müller et al. 2011) and 0.037 ± 0.002 (Abe et al. 2008) have been reported, with most recent estimates being $p_V = 0.047 \pm 0.003$ (Ishiguro et al. 2014). The bond albedo was reported to be $A_B = 0.014 \pm 0.002$ (Ishiguro et al. 2014), commensurate with the values for common C-type asteroids. The effective diameter of 1999 JU3 is 0.92 $\pm$0.12 km (Müller et al. 2011), and the minimum and maximum radii are reported to be 374 and 495 m, respectively. This estimate is close to previously published values, which are diameters of 980 ± 29 m (Abe et al. 2008) and 900 ± 140 m (Campins et al. 2009). The spin period of the asteroid is 7.63$\pm$0.01 h (Müller et al. 2011).

The surface thermal inertia Γ of 1999 JU3 has been derived using a thermal model and mid-infrared telescopic observations, and reported values range from 200 to 600 J

m^{-2} K^{-1} $s^{-1/2}$ (Hasegawa et al. 2008; Müller et al. 2011). However, values towards the high end of this range are more likely, and a lower bound of 500 J m^{-2} K^{-1} $s^{-1/2}$ has been reported (Hasegawa et al. 2008) with a rigorous lower limit of 150 J m^{-2} K^{-1} $s^{-1/2}$ (Campins et al. 2009). Thus, thermal inertia is about a factor of two lower than that of 25143 Itokawa (Müller et al. 2011), indicating that surface texture lies somewhere between a thick-dust regolith and a gravel-dominated surface, where thick means large with respect to the diurnal thermal skin depth of ∼10 cm. This is in line with the observation that thermal inertia of NEAs can be approximated empirically by a fitting function of the form $\Gamma = d_0 D^{\zeta}$, where D is the diameter of the object and d_0 as well as ζ are fitting parameters. Using this formula, Delbo et al. (2007) derive thermal inertias close to 300 J m^{-2} K^{-1} $s^{-1/2}$ for a km size NEA such as 1999 JU3. As a comparison, a thermal inertia of 500 J m^{-2} K^{-1} $s^{-1/2}$ is considerably larger than that reported for dust (∼30 J m^{-2} K^{-1} $s^{-1/2}$, e.g., Putzig et al. (2005)) or the lunar regolith (∼50 J m^{-2} K^{-1} $s^{-1/2}$, e.g., Spencer et al. (1989)), but close to that reported for coarse sand (∼400 J m^{-2} K^{-1} $s^{-1/2}$, e.g., Mellon et al. (2000)). It is, however, considerably smaller than that of bare rock (> 2500 J m^{-2} K^{-1} $s^{-1/2}$, e.g., Jakosky (1986)) and metal rich asteroidal fragments (∼12000 J m^{-2} K^{-1} $s^{-1/2}$, e.g., Farinella et al. (1998)).

Information on the surface texture of C type asteroids is sparse, and 253 Mathilde is the only C-type that has been visited by spacecraft to date. Except for the lower geometric albedo (0.047 ± 0.005), the photometric properties of Mathilde are closely similar to those of the Martian moon Phobos, and the surface is extremely homogeneous in terms of both color or albedo. In particular, no color or albedo variations associated with craters have been identified (Veverka et al. 1999). However, due to the limited image resolution even at closest approach of approximately 1200 km, little is known about the detailed surface structure of C-type asteroids, and thermal inertia currently is the only means to learn about rock distribution and estimated regolith thickness.

The present day estimates of the thermal inertia of 1999 JU3 are compatible with a surface covered predominantly by boulders and bare rocks, while areas with dusty regolith should be less common. Mid-infrared observations indicate that a thick regolith layer can be excluded (Hasegawa et al. 2008), and a rather thin (mm scale) regolith layer is predicted (Hasegawa et al. 2008). As compared to the Hayabusa 1 target asteroid Itokawa, the surface of 1999 JU3 is expected to have fewer rocks and boulders, and the surface likely includes millimeter sized particles, as opposed to the cm-sized gravel on Itokawa, which has a regolith thickness of 42 ± 1 cm (Barnouin-Jha et al. 2008). Thermal history calculations for likely orbits of 1999 JU3 indicate that the asteroid's surface has experienced only moderate temperatures of at most 500 K, and that pristine material which has not been heated above 450 K should be present at depths of only 3 cm (Michel and Delbo 2010). Thus, it is very likely that the samples to be collected by Hayabusa 2 will have components that will be thermally unaltered as long as some of it comes from depths of at least 3 to 5 cm (Michel and Delbo 2010).

The primary scientific goal of the MARA instrument is the determination of the surface thermal inertia by means of determining the surface brightness temperature at the landing sites for a full asteroid rotation. Measurements during night-time are particularly suited to determine thermal inertia, as night-time temperature drift is largely independent of surface emissivity and albedo, which dominate the daytime surface energy balance. In addition, while thermal inertia determined over large spatial scales gives a non-linear average of the surface thermo-physical properties, with hotter surfaces being overrepresented, the small field of view of the MARA instrument will

enable a local estimate of the thermo-physical properties of the regolith. A secondary goal of the MARA instrument is the characterization of the surface mineralogy using its four bandpass channels, and the spectral slope in the wavelength range between 5.5 and 15.5 µm will be determined. This can help to identify some phyllosilicates (Grott et al. 2013), and MARA will thus provide data that can help to refine the classification of 1999 JU3 between the Cg and Ch/Cgh subtypes, complementing measurements in the 0.95 to 3.65 μm wavelength range performed by MicrOmega (Bibring et al. 2015). Finally, one channel of the MARA instrument is identical to that used by the spacecraft thermal mapper (Okada et al. 2012), and will serve as ground truth for measurements at spacecraft altitude. A science traceability matrix putting the MARA science objectives into the larger Hayabusa II context is given in Table 1, and in the following we will present the detailed design of the instrument as well as the instrument calibration and key performance characteristics.

2.2 Design Overview

Development of the MASCOT radiometer MARA is driven by the need to find a compromise between the science requirements outlined in Sec. 2.1 and the limited resources in terms of mass, volume, and power which are available on a small lander such as MASCOT. In addition, the short development timescale forces the design to heavily draw on previous developments like MUPUS-TM and the MERTIS radiometer. Technically, design drivers for MARA were found to be the physical separation of sensors and readout electronics (MERTIS heritage, Hiesinger et al. (2010)), the need to stabilize the sensor head operating temperature (MUPUS-TM heritage, Spohn et al. (2007)), the sensor design (MUPUS-TM heritage), and the limitation of the instrument's field of view. Concerning temperature stabilization, limited engineering resources did not allow for an active cooling of the sensor head to be implemented, and MARA relies on heating the instrument above ambient temperatures, while cooling is achieved by radiating heat to the environment. Therefore, a compromise between efficient cooling and the need to conserve energy needed to be found.

The MARA sensor head (left panel in Fig. 1) houses 6 thermopile sensors, each observing the surface in a dedicated wavelength band. The instrument's field of view is limited by the aperture cover to 18° (full width half maximum), and the interior baffle is black coated with emissivity 0.95 to eliminate stray light. Sensor viewing directions are collocated within the MASCOT camera field of view (Jaumann et al. 2015), such that the surface texture of the observed surface will be known during data interpretation. This is important since non-resolved surface roughness in the field of view can significantly influence the emitted flux, and care must be taken during data analysis (Davidsson et al. 2015). For nominal landing conditions, the 18° field of view translates to a MARA footprint size of 12 cm, while the mounting of MARA results in average emission angles of 50°.

Surface coating of the sensor head was chosen for high reflectivity to keep the instrument cool, as well as low emissivity to conserve heating power while keeping the temperature stabilized at the instrument's operation setpoint. The applied gold coating has an emissivity of 0.05 at 3µm, which gradually increases to 0.12 at 10µm. In order to further minimize heat losses from the sensor head, thermal insulation stand-offs and a flex harness have been implemented, which drastically increases thermal resistance when compared to traditional round wire cables. The sensor head heater is integrated

Table 1 Science traceability matrix showing the overarching Hayabusa II science goals as well as those objectives to which MARA directly or indirectly contributes by measuring net radiometric fluxes in the different passbands.

Goal 1: Understand how materials evolved in the early phases of the solar system and how they have been altered at later times on the asteroid.

Hayabusa II Objective	MASCOT Objective	MARA Measurements
1.1) Describe how materials of different characteristics are distributed on the asteroid.	1.1a) Characterize the mineralogical composition of the surface and near-surface material.	1.1a) Constrain regolith mineralogy by estimating surface emissivity.
	1.1b) Characterize the local morphology and in-situ structure and texture of the regolith.	1.1b) Constrain surface texture by estimating surface thermal inertia and surface roughness.
1.2) Analyze returned samples from a microscopic standpoint combined with a macroscopic view given by the remote sensing data.	1.2) Provide context of the samples collected and returned by the main spacecraft	1.2) Constrain surface texture by estimating surface thermal inertia and surface roughness. Constrain mineralogy by estimating emissivity.
1.3) Decipher the later thermal evolution that must have obscured some of the early memories.	1.3a) Characterize the surface thermal environment	1.3a) Determine the surface brightness temperature.
	1.3b) Characterize the regolith thermo-physical properties.	1.3b) Estimate surface thermal inertia, roughness, and emissivity.

Goal 2: Understand the dynamical evolution and the resultant structure of the asteroid as a possible analogue for construction of planetesimals.

Hayabusa II Objective	MASCOT Objective	MARA Measurements
2.1) Characterize the collisional fragmentation-accretion history of the asteroid.	2.1) Characterize the body constitution on local and/or global scales and constrain surface and possibly subsurface physical properties.	2.1) Constrain surface texture by estimating surface thermal inertia and surface roughness.

into the sensor head's printed circuit board (PCB), which provides electrical connection to the instrument's backend electronics situated in the lander's warm electronics box. Heating coils in the PCB are routed in a bifilar manner to minimize the generation of magnetic fields and thus disturbances to the magnetometer (Herzig et al. 2015). The flex harness is part of the sensor head PCB, and it is fully shielded to reduce electronics noise.

During cruise, MARA views an on-board calibration target (top right panel in Fig. 1), to check instrument calibration and correct for any potential longterm drift of sensor sensitivity or electronics. The surface viewed by MARA is black coated and micro-structured for maximum emissivity, and an emissivity of 0.99 is achieved in the wavelength range of 5-10 µm, while emissivity is 0.95 in the range 10-40 µm. Major engineering budgets and key performance characteristics of the instrument are summa-

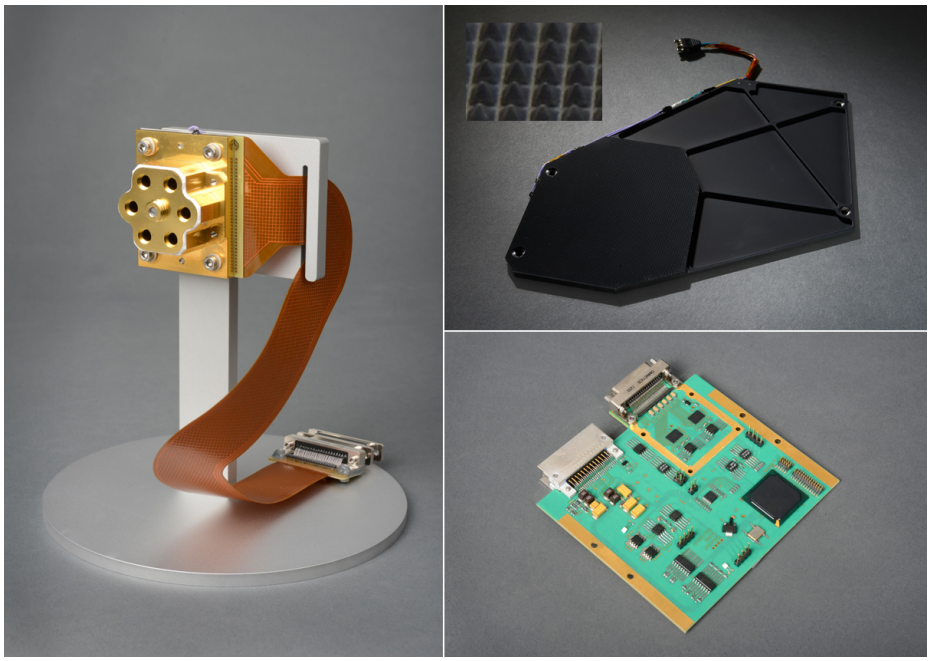

Fig. 1 Left: Sensor head including the shielded flex harness mounted to a holding fixture. Top right: On-board calibration target. The micro-structured region in the bottom left corner covers the MARA field of view, the area to the upper right is in the field of view of the MASCOT camera (Jaumann et al. 2015) and used for dark current measurements. Micro-structures are shown in the inset. Bottom right: MARA backend electronics.

rized in Table 2. It is worth noting that minimum expected night-time temperatures depend on season and landing site latitude, but are expected to be above 150 K (compare, e.g., Takita et al. (2015)) even for low thermal inertia of 250 J m^{-2} K^{-1} s$^{-1/2}$. Therefore, performance in the long-pass channels is fully sufficient to obtain surface brightness temperatures for an entire day-night cycle.

2.3 Measurement Principle

MARA measures the net radiative flux exchanged between the sensing element and the surface in the field of view by determining the temperature of an absorbing surface with respect to a reference temperature. The temperature measurement is performed by a stack of thermo-elements (so called thermopiles) which convert temperature differences to electrical potential differences by means of the Seebeck effect. The amount of radiation emitted by a surface of emissivity ϵ at temperature T and received by the instrument is given by

$$F_{in} = \pi\nu \int_{\lambda_1}^{\lambda_2} H(\lambda)\epsilon B_\lambda(T)d\lambda$$

where ν is solid angle covered by the target (the viewfactor), λ is wavelength, and $H(\lambda) = \tau(\lambda)\epsilon_{Abs}(\lambda)$ is the instrument function (throughput) given by the product of

Table 2 Instrument overview giving the major engineering budgets as well as the key performance characteristics. Power uptake of the instrument is driven by the heating power required to maintain the instrument at the operating setpoint. [1]Heating power varies according to the environmental conditions. [2]Temperature uncertainty is a function of the target temperature and spectral channel. [3]NETD: Noise equivalent temperature difference.

Property		Value	Units
Mass	Sensor Head incl. Harness	83	g
	Electronics	113	g
	Calibration Target incl. Harness	117	g
Size	Sensor Head	54 x 48 x 26	mm^3
	Electronics	152 x 152 x 5	mm^3
	Calibration Target	109 x 94 x 14	mm^3
Operating Temperature	Sensor Head	173 to 385	K
Range	Electronics	233 to 343	K
	Calibration Target	173 to 358	K
Power Uptake	Standby Mode	0.22	W
	Science Mode	0.31	W
	Calibration Mode	0.31	W
Heating Consumption[1]	Sensor Head	0 to 2	W
	Calibration Target	0 to 2	W
Spectral Range	Bandpasses	5.5-7, 8-9.5	µm
		9.5-11.5, 13.5-15.5	µm
	Broad Bandpass, Longpass	8-12, > 3	µm
Calibration	Temperature Range	123 to 373	K
Temperature Uncertainty[2]	Bandpasses at $T > 273$ K	1	K
	> 3 µm channel at $T > 173$ K	1	K
	8-12 µm channel at $T > 173$ K	1.5	K
Noise	Electronics	15	nV
	Thermal	60	nV
NETD[3]	Bandpasses at $T > 273$ K	0.1	K
	> 3 µm channel at $T > 123$ K	0.1	K
	8-12 µm channel at $T > 123$ K	0.2	K
Field of View	Full Width Half Maximum	18	°
Measurement Frequency	Science and Calibration Mode	1/30	Hz
Data Volume	Science	20	bit/s
	Housekeeping	8	bit/s

the absorbing characteristics of the sensing element ϵ_{Abs} and the transmission $\tau(\lambda)$ of the applied filter. B is the Planck function. At the same time, the instrument re-radiates flux at the instrument temperature T_{ref}, such that the net flux onto the absorber is given by

$$F_{net} = \pi\nu \int_{\lambda_1}^{\lambda_2} H(\lambda) \left(\epsilon B_\lambda(T) - B_\lambda(T_{ref}\right) d\lambda$$

It should be noted that strictly speaking the instrument will radiate at the (unknown) absorber temperature T_{abs}, but given that the maximum expected temperature difference across the thermopile sensor is below 0.1 K, it can be assumed that $T_{abs} = T_{ref}$ to good approximation. Nevertheless, the most precise measurements will be obtained when target and sensorhead are at the same temperature. In this case, T_{ref} directly measures the temperature of the surface in the field of view while the resulting signal is zero.

Usually, the solid angle ν filled by the target surface will be small when compared to the viewfactor of the sensor housing ν_H, and an additional self-radiation term

$$F_H = \epsilon_H \pi \nu_H \int_0^\infty \left(B_\lambda(T_H) - B_\lambda(T_{ref}) \right) d\lambda$$

needs to be taken into account, where ϵ_H is the housing emissivity and T_H the housing temperature. Total flux onto the absorber is then given by $F_{tot} = F_{net} + F_H$, and care must be taken to properly account for F_H during instrument calibration. For MARA, the sensor head temperature is stabilized such that $T_H \approx T_{ref}$, and the self radiation term is thus minimized with respect to the desired signal. Residual fluxes associated with thermal gradients across the instrument are accounted for during calibration by considering a heating current dependent signal offset, which is linear to a very good approximation (cp. Sec. 3.1).

Ignoring self radiation for further discussion, the thermal voltage U_{th} generated at each sensor is then a function of the sensor sensitivity S (in units of V/W), the absorber size A_d, the emissivity of the emitting surface ϵ, the viewfactor of the surface ν, the instrument throughput $H(\lambda)$, as well as the temperature of the target surface T and the reference junction temperature T_{ref}. Signal strength is then given by

$$U_{th} = S A_d \pi \nu \int_{\lambda_1}^{\lambda_2} H(\lambda) \left(\epsilon B_\lambda(T) - B_\lambda(T_{ref}) \right) d\lambda$$

and it needs to be kept in mind that MARA (like any bolometer) only measures net fluxes exchanged between instrument and target surface. Therefore, care must be taken when interpreting the target temperature T in terms of surface brightness temperature.

2.4 Sensor Design

MARA uses the IPHT TS-72M thermopile sensors as sensing elements (Kessler et al. 2005), which consist of 72 n-bismuth-antimony/p-antimony (Bi0.87Sb0.13/Sb) thermocouples with a Seebeck coefficient of 135 µV/K each. The incoming radiation is coupled into a circular absorber of 0.5 mm diameter, and the signal voltage is generated by the temperature difference between hot and cold junction of the thermopile due to the Seebeck effect. PT100 platinum resistance thermometers measure the thermopile cold junction temperature T_{ref} as a reference. Thermopiles and PT100 sensors are mounted on standard TO-39 metal can sockets, and electrical connection to the terminals is provided by bond wires, which are redundant where space permits. Thermopiles are designed such that sensors have a center tap, which is used to bias the thermopile voltage to the applied reference voltage of 2.5 V. Thermopiles have a nominal resistance of 20 kΩ, giving 10 kΩ per thermopile leg. Aperture holes are laser-cut into the TO-39 caps, and IR filters are glued to the housing, which is coated black on the inside to reduce stray-light and limit the sensor's field of view. Fig. 2 shows the MARA sensors mounted inside the sensor head (left panel), where the aperture cover has been removed to better view the sensors. The interior layout of the sensors is shown in the right panel of the same figure, showing the thermopile absorber, the PT100 sensor, as well as the bond wires including the mid-tapping on the top-left corner of the chip.

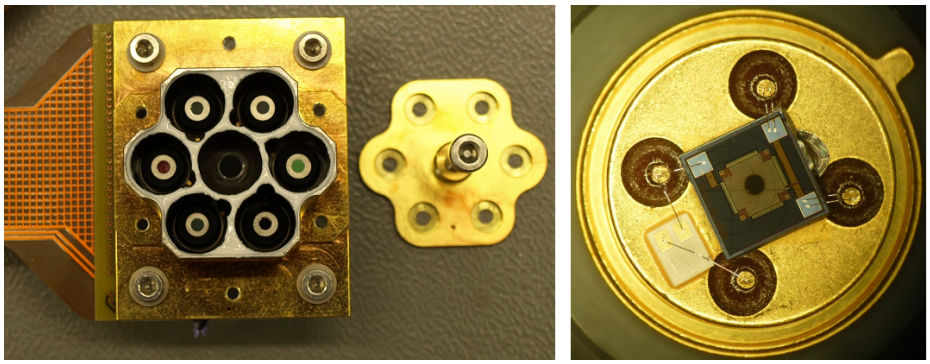

Fig. 2 Left: Sensorhead with aperture cover removed. Baffles of the six thermopile sensors are coated black to eliminate stray light. Right: Thermopile sensor with the cap including the filter window removed. The absorbing surface is coated black (middle of the image) and connected by bond wires to the housing. A PT100 sensor (towards the lower left) measures the housing (cold junction) temperature.

Sensors are encapsulated under Xenon fillgas, which has a boiling point of 165 K and limits the non-operational storage temperature of the sensors (the employed absorbers have storage temperatures down to 143 K). Xenon has been chosen over the standard Krypton fillgas, which boils at 121 K because of its larger molecular weight, which results in a lower thermal conductivity, thus increasing sensor sensitivity by a factor of 1.3 to 1.5 when compared to Krypton. Ideally, sensors would be encapsulated under vacuum, thus further reducing thermal conductivity, but it is difficult to guarantee sensor stability during assembly and launch operations. MUPUS-TM sensors were encapsulated using venting holes, but this requires intricate purging by dry N_2 during handling under Earth ambient conditions.

Filters of the MARA instrument have been chosen in accordance with the science goals outlined in Sec. 2.1 and a long-pass channel is dedicated to the determination of the asteroid's surface brightness temperature and optimized for maximum signal to noise. Given that 99% of the signal will be from reflected sunlight for wavelengths smaller than 3.5 µm, the filter was chosen to open up around this wavelength, while collecting flux up to at least 100 µm. A second broad bandpass was chosen to be similar to that employed by the Hayabusa 2 orbiter thermal imager (Okada et al. 2015), collecting flux in the classical 8-12 µm band. Four band passes with transmission in the 5.5-7, 8-9.5, 9.5-11.5, and 13.5-15.5 µm wavelength range will be used for determining spectral slope in the thermal infrared.

Usually, IR filters become transparent at around twice the wavelength of the optical window, and, in addition, Germanium based filters generally become transparent at $\lambda > 50$ µm. As a significant part of the signal can originate at wavelength > 50 µm for low night time temperatures, this signal needs to be blocked. MARA achieves this by using the IPHT interference absorbers, and the absorptivity of the sensors is shown in the top left panel of Fig. 3 as a function of wavelength. As an example for the combined throughput of the filter-absorber combination, the transmission of the 5.5-7 µm filter is shown together with the short wavelength interference absorber absorptivity as a function of wavelength. The absorber efficiently suppresses the transmission bands around 10-20 µm as well as the Germanium transparency feature at $\lambda > 50$ µm.

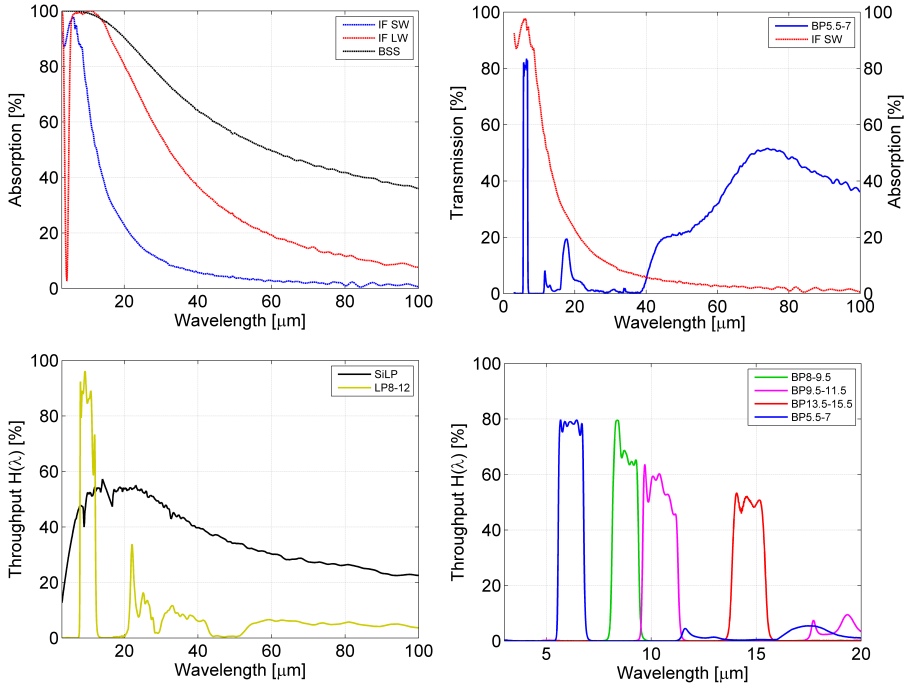

Fig. 3 Top Left: Absorption as a function of wavelength for the different employed absorbers. Results are shown for the short (IF SW) and long wavelength (IF LW) interference absorbers as well as the black silver smoke absorber (BSS). Top Right: Example of the combination of transmission for the 5.5-7 µm filter (BP5.5-7) and absorption for the short wavelength interference absorber (IF SW). Bottom Left: Throughput of the porous silicon longpass filter (SiLPi) as well as the 8-12 µm filter (LP8-12). Filters are combined with the black silver smoke absorber (BSS). Bottom Right: Throughput of the 5.5-7 (BP5.5-7), 8-9.5 (BP8-9.5), 9.5-11.5 (BP9.5-11.5), and 13.5-15.5 µm filters (BP13.5-15.5). Absorber combinations are given in the figure legend.

Filter transmission characteristics have been determined in DLR's Planetary Emissivity Laboratory (PEL) at the Institute for Planetary Research. Spectra were obtained using an evacuated (10^{-4} bar) Bruker Vertex 80V FTIR spectrometer coupled with an external evacuated emissivity chamber. To cover the 1 to 16 µm spectral region spectra were measured using a nitrogen cooled detector MCT and a KBr beamsplitter. The combined filter transmission and thermopile absorption (the instrument throughput) is shown in the lower panels of Fig. 3, where the temperature channels are given on the left hand side, while the narrower bandpasses are given on the right.

Filter characteristics as well as the employed absorbers are summarized in Table 3, and chosen substrate as well as the employed fillgas are shown. Furthermore, the main measurement objective for each channel is also given. Note that the choice of the BSS absorber for the LP8-12 filter was motivated by the fact that throughput for this channel should be spectrally similar to the filter employed for the Hayabusa II orbiter TIR instrument. It is also worth pointing out that no degradation of filters is expected as a result of their exposure to the space environment, and no degradation has been observed for the MUPUS-TM filters during Rosetta's 12 year cruise(Spohn et

Table 3 Filter-absorber combinations used in the MARA instrument. Absorber designations are IF LW, IF SW, and BSS for long wavelength and short wavelength interference absorbers as well as black silver smoke absorbers, respectively. BP: Bandpass, LP: Longpass, SiLP: Silicon longpass.

Name	Range [µm]	Absorber	Fillgas	Substrate	Main Objective
BP5.5-7	5.5-7	IF SW	Xenon	Ge	Spectral emissivity
BP8-9.5	8-9.5	IF SW	Xenon	Ge	Spectral emissivity
BP9.5-11.5	9.5-11.5	IF SW	Xenon	Ge	Spectral emissivity
BP13.5-15.5	13.5-15.5	IF LW	Xenon	Ge	Spectral emissivity
SiLP	> 3	BSS	Xenon	Si	Surface brightness temp.
LP8-12	8-12	BSS	Xenon	Si	Surface brightness temp. / TIR ground truth

al. 2007, 2015). The same holds for the thermopile detectors, for which no degradation was observed as a result of total ionizing dose or single events displacement damage. Furthermore, even if degradation would occur, this could be recalibrated using the on-board calibration target, and no further degradation would be expected during MASCOT's 16 h science mission.

2.5 Electronics Design

The MARA instrument consists of three functional subunits comprising the sensor head, calibration target, and backend electronics (bottom right panel in Fig. 1), which interface with the lander on-board computer (OBC). A schematic block diagram of the MARA instrument is shown in Fig. 4 with the backend electronics on the left hand side, the sensor head at the top right, and the calibration target at the lower right. All active electronics parts are located on the MARA backend electronics board, and MARA operation is controlled by the instrument's FPGA. The FPGA operates the analogue to digital converters (ADCs) as well as the proportional-integral-controller (PI-controller) used to stabilize temperature of sensor head and calibration target. In order to minimize disturbances to the magnetometer, the FPGA pulse-width modulated control signal for the PI-controller is low pass filtered to generate an analogue voltage, which is then used to regulate the applied heating currents. Sensor head and calibration target house thermopiles, PT100 temperature sensors, and heaters for temperature control, but signals are converted in the backend electronics only.

The MARA signal processing chain is direct heritage from the MERTIS radiometer (Hiesinger et al. 2010) and the science data acquisition unit is built around the commercial LTC2449 24bit analogue to digital converter (ADC), which has been upscreened for application on the Bepi Colombo mission. Being susceptible to single event latchups, a latchup protection circuit has been implemented in hardware to switch of the ADC in case an overcurrent is detected. The ADC houses a multiplexer for sequential reading of 8 differential input channels as well as external terminals for signal conditioning. MARA uses the ISL70227 operational amplifier, which features very low bias currents at low noise, and signals are amplified at a gain of 43.5, limited by the PT100 signals. ADCs as well as the bias voltage for the thermopiles and PT100 sensors are supplied by a common REF43S precision 2.5V voltage reference, such that

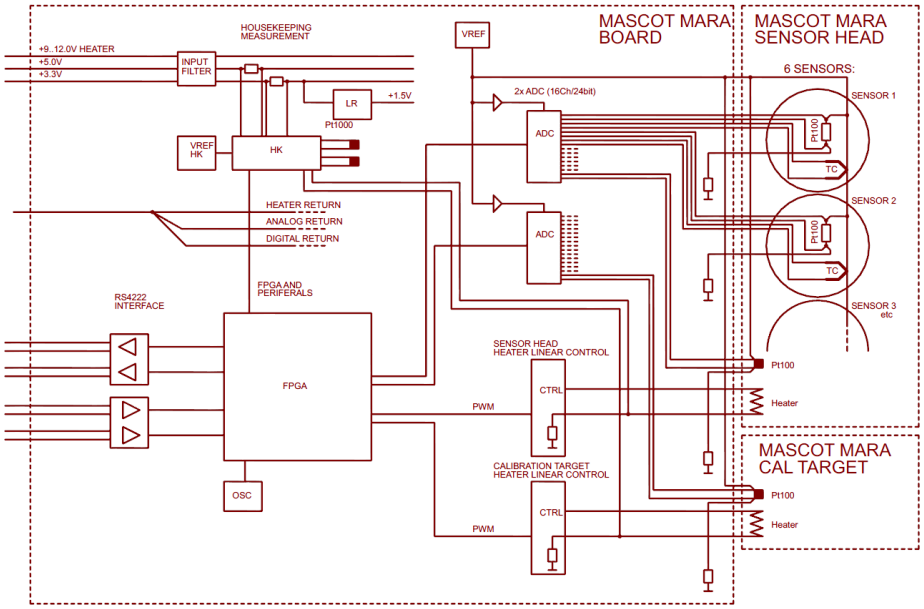

Fig. 4 Functional block diagram of the MARA instrument showing the three functional units: The MARA backend electronics (MARA board), the sensor head, as well as the on-board calibration target. Pt100: Platinum temperature sensor, TC: Thermocouple.

temperature drift of the reference is largely eliminated. PT100 sensors are referenced to low drift and high precision resistors to further eliminate electronics drift from the measurements.

MARA uses two LTC2449 ADCs to convert signals from 6 thermopiles, 6 sensor head PT100 sensors, as well as the two 100 Ω reference resistors. In addition, two PT100 sensors used for temperature control are also converted using the science ADCs. Other housekeeping (HK) measurements are performed using dedicated HK converters. In order to avoid cross-talk between the ADCs, two independent measurement systems including individual reference voltages and reference resistors have been implemented. Performance of the electronics design is shown in Fig. 5, where the noise on the thermopiles (left panel) as well as noise on the PT100 sensors (right panel) is shown. Noise of the electronics itself has been determined from the 100 Ω reference resistors, and was found to be less than 15 nV using an integration time of 1 s per channel (not shown). Sensor noise is dominated by thermal noise caused by the imperfect temperature regulation, and is close to 60 nV for all sensors. In the steady state, the implemented PI-controller stabilizes the sensor head temperature to within 1 mK.

2.6 Instrument Operations

The MARA instrument can be operated in one of three operation modes: Standby, calibration, and science mode. In standby mode, only the FPGA, the HK ADCs, and the telemetry interfaces are powered on, while science ADCs and heaters are powered off. This is the operation mode following switch-on, and direct commanding is required

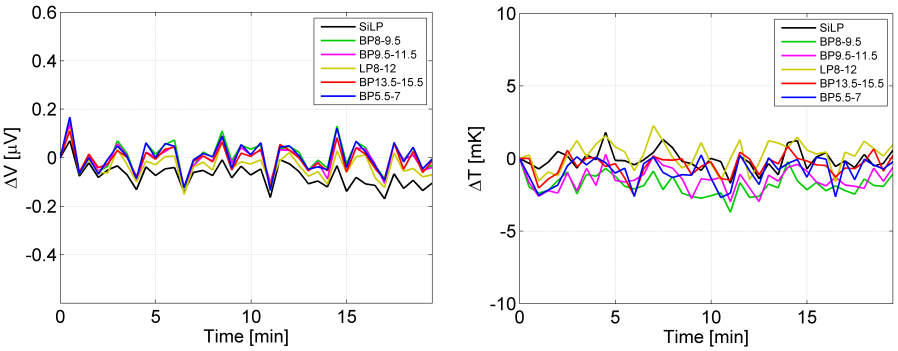

Fig. 5 Left: Thermopile signal as a function of time as measured during calibration. Sensor head temperature is equilibrated at 298 K, and sensors are viewing a cavity blackbody at T_{BB} = 208 K. Thermopile noise is close to 60 nV for all sensors, dominated by thermal noise. Right: Thermal noise for the same data. Temperature is stable to within 1 mK in the equilibrated state.

for the instrument to obtain science data and operate the PI-controller for temperature equilibration of the sensor head and calibration target.

Calibration mode is used during cruise extended checkouts, and all functional subunits including the temperature controllers for sensor head and calibration target are switched on. In this mode, science data vectors containing readings of the thermopiles, PT100 sensors, and reference resistors are acquired sequentially at integration times of 1 s per channel, such that a data vector is produced within 16 s. Acquisition of all channels is repeated every 30 s. During calibration, the instrument sensor head is equilibrated at the operation setpoint, while the calibration target temperature is increased stepwise from its initial temperature. In this way, sensitivity and heating induced offsets can be determined and compared to the ground calibration (cp. Sec. 3.1).

During science operations, data acquisition is identical to that in the calibration mode, but the calibration target control circuitry remains switched off, as the calibration target will remain on the Hayabusa 2 spacecraft after separation. The nominal operation scenario foreseen for MARA consists of preheating the sensor head while still powered via the Hayabusa 2 bus to conserve energy in the MASCOT primary batteries. The instrument then remains switched on during separation, descent, and landing, taking science data at 30 s intervals for a 16 h period until the end of the mission.

3 Instrument Calibration

3.1 Radiometric Calibration

MARA has been calibrated in the space simulation chamber at DLR using a low temperature (100-400 K) cavity blackbody (BB100, Sapritsky et al. (2003)) with emissivity of 0.999 as calibration source, and the calibration setup is schematically shown in Fig. 6. The instrument was mounted in a thermal enclosure reproducing the thermal characteristics of the lander interface as closely as possible. Calibration was carried out under

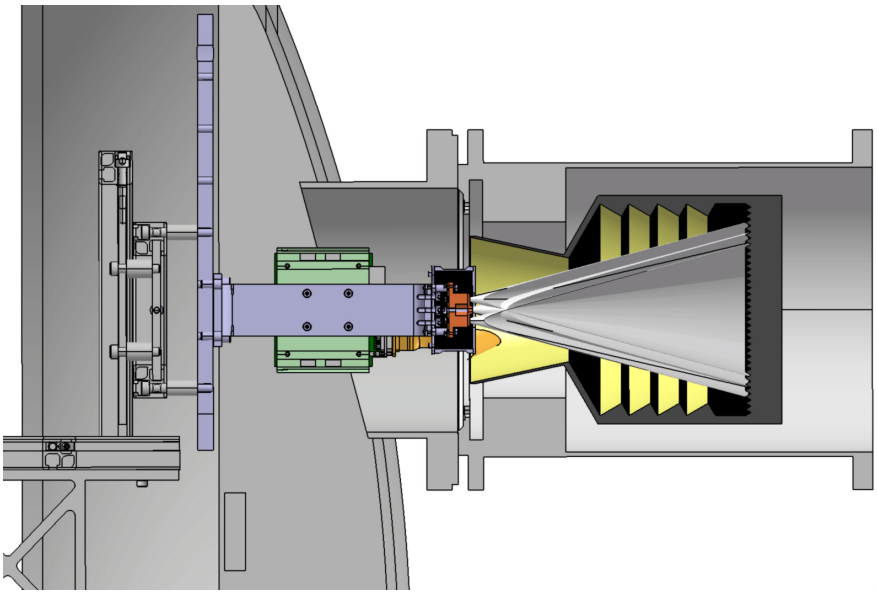

Fig. 6 Schematic setup of the radiometric calibration. The instrument sensor head (orange) is mounted in a thermal enclosure, which simulates temperatures in the MASCOT payload compartment. Mounting of the sensor head uses thermal stand-offs to mimic the thermal contact of the instrument to the MASCOT lander. Fields of view of the individual sensors are indicated, and sensors view the baseplate of the cavity blackbody (yellow/black). The temperature of the instrument's electronics board is separately controlled (green).

vacuum conditions with typical pressures around 10^{-5} bar, and the MARA sensors were viewing the cavity blackbody as indicated in the figure. Spatial homogeneity of the incident radiation was verified by moving the instrument with respect to its center position without a change of signal.

The instrument has then been calibrated at 3 operation setpoints of 273, 298, and 323 K, and for each setpoint a two-step calibration procedure was carried out: First, while keeping the instrument temperature stable using the instrument's PI temperature controller, the blackbody temperature was stepwise increased from 123 K to 373 K. The resulting thermopile signal is shown in the left panel of Fig. 7, where U_{th} is given as a function of net radiative power P for the calibration run at a sensor head temperature of 298 K. As a second step, sensor head and blackbody were equilibrated at the same temperature while changing the temperature of the instrument's thermal enclosure. Keeping the sensor head temperature stable then requires different heating powers P_H, which result in small thermal gradients across the instrument and give rise to offset voltages (cp. the discussion on F_H in Sec. 2.3). Results of this offset calibration are shown in the right panel of Fig. 7, where ΔU_{th} is given as a function of applied heating power P_H.

The data gained during the calibration was then reduced to four calibration coefficients by first determining the slope of the ΔU_{th} vs. P_H curve to determine S_H by

$$S_H(P_H) = \frac{\partial \Delta U_{th}}{\partial P_H}$$

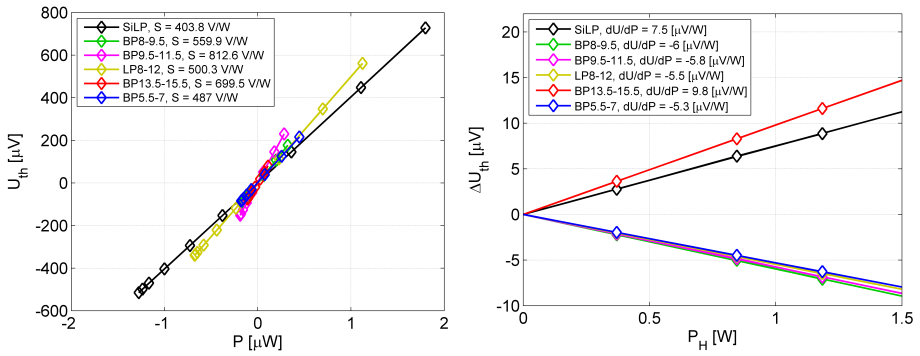

Fig. 7 Results of the radiometric calibration. Left: Thermopile voltage as a function of net radiative power. Sensitivity of the individual sensors is given in the legend. Right: Offset thermopile voltage as a function of instrument heating power. A linear fit to the data is also shown.

The data obtained during the calibration of U_{th} vs. received net power $P = F_{net}A_d$ was then corrected for this offset, and the residual signal was fitted to a second order polynomial with free parameters S, S_1, and S_2, i.e.,

$$U_{th} - S_H(P_H)P_H = SP(T_{BB}, T_{ref}) + S_2P(T_{BB}, T_{ref})^2 + S_1$$

Note that the net power incident on the absorber is a function of both T_{BB} and T_{ref} as discussed in Sec. 2.3. In this way, fitting residuals below 1 µV have been obtained across all sensors, with S dominating the fit. This is also evident from the almost linear relationship between U_{th} and P expressed in the left panel of Fig. 7.

Calibration was repeated for all operation setpoints and similar results to those shown in Fig. 7 have been obtained. Due to the temperature dependence of the fillgas thermal conductivity sensor sensitivity is also a function of temperature. Lower sensor temperatures result in lower conductivities and thus larger sensitivities, and a sensitivity temperature drift between 0.43 and 0.51% K^{-1} has been observed for the different sensors.

3.2 Geometric Calibration

The field of view of the MARA sensors has been determined using a collimated blackbody source at $T_{BB} = 1000$ K in conjunction with a pan-tilt unit on which the instrument was mounted during testing. Starting from viewing angles of -20°, the sensor head was tilted in increments of 0.5°, until the final position of +20° was reached. At each stop, measurements with and without a shutter were made to eliminate the non-constant background radiation, which was later subtracted during data analysis. This procedure was carried out twice, once in the horizontal direction (azimuth determination) and once in the vertical direction (elevation determination).

Results of these measurements are shown in Fig. 8 for the SiLP filter, where the left panel shows the thermopile voltage as a function of azimuth, whereas the right panel shows U_{th} as a function of elevation. Results are similar for the other filters, albeit at a lower signal-to-noise. Sensors collect signal to angles of about 15° off-axis, and the full-width half-maximum field of view is 18°.

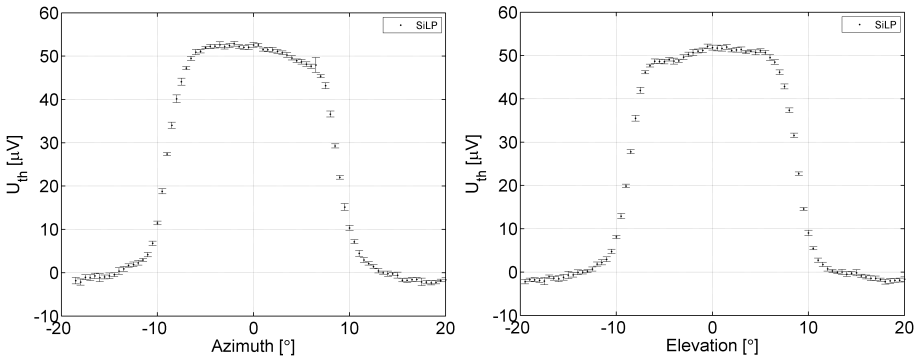

Fig. 8 Thermopile signal as a function of viewing angle for the SiLP filter. The standard deviation at each measurement point is indicated by errorbars. Azimuth (left) as well as elevation (right) have been varied. Results for the other filters are similar, but show larger noise due to their decreased sensitivity in the relevant wavelength range.

3.3 Verification Measurements

Verification of the radiometric calibration was carried out using three different approaches: First, the reproducibility of the calibration measurements (cp. Sec. 3.1) was tested by re-running part of the calibration sequence, and reproducibility was found to be better than 1 K over the entire calibration range (123 to 373 K) for the SiLP and 8-12 µm Filters. Due to the lower signal to noise, reproducibility in the bandpass filters was only 2-3 K for the 9.5-11.5 and 13.5-15.5 µm bandpasses, while it is 5-6 K for the short wavelength 5.5-7 and 8-9.5 µm bandpasses, which receive even less signal at low temperatures. However, even in the bandpasses, reproducibility was found to be better than 1 K for target temperatures above 273 K.

As a second step, the calibration was verified by choosing blackbody target temperatures in-between the original calibration points, thus testing the capability of the instrument calibration model (Sec. 3.1) to interpolate results to unknown fluxes. Results were essentially found to be identical to the reproducibility measurements discussed above, indicating that signal-to-noise as well as heater induced offsets are the main source of uncertainty in the measurements.

Finally, in order to estimate the performance of the instrument under non-constant ambient conditions, a verification measurement simulating on-asteroid operations has been performed. During the measurement, ambient temperatures have been varied between228 and 293 K, which is the temperature range for the MARA sensor head as predicted by the MASCOT engineering thermal model for on-asteroid operations. The MARA sensor head was temperature stabilized at 298 K, thus imposing varying residual thermal gradients across the instrument during the test. Target blackbody temperature was varied between 173 K and 373 K, and the ambient temperature T_{AMB}, blackbody temperature T_{BB}, as well as the heating power P_H required to stabilize the sensor head at its operation setpoint are shown in the left panel of Figure 9.

Measured thermopile voltages were corrected for heating induced offsets as described in Sec. 3.1, and the inverted temperatures were compared to the known blackbody temperatures. The temperature difference ΔT between the two is shown in the right panel of Fig. 9 as a function of target temperature T_{BB}. Temperature residuals

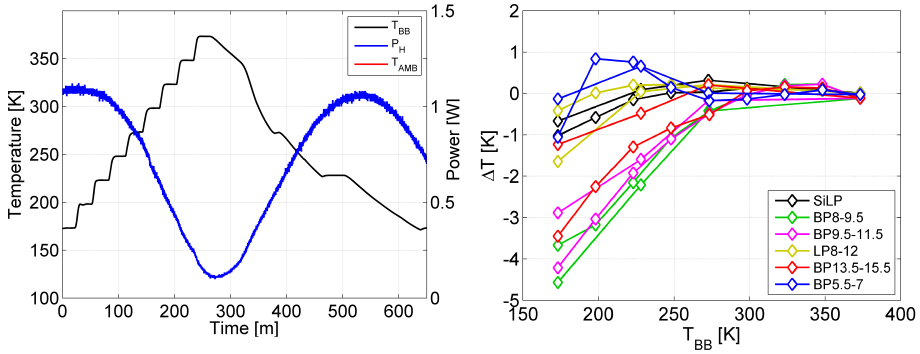

Fig. 9 Left: Blackbody temperature (black), instrument ambient temperature (red), as well as the heating power (blue) needed to stabilize the instrument temperature as a function of time. Temperatures are given on the left ordinate, while power is shown on the right. During the verification run, the sensor head temperature was kept stable at 298 K. Right: Temperature difference ΔT between the target temperatures as determined by MARA and the actual temperatures of the blackbody source T_{BB}. Measurements have been taken at the temperature plateaus to guarantee thermal equilibration of the blackbody source during the heating as well as during the cooling parts of the curve.

for the SiLP longpass filter are below 1 K, indicating that temperatures down to 173 K can be measured with this uncertainty. Furthermore, uncertainty in the 8-12 µm and 13-15 µm bandpass filters is better than 2 K, while the narrow bandpasses only give good signal to noise at target temperatures above 273 K.

These results demonstrate that the offset correction applied during calibration can account for residual thermal gradients across the instrument, thus effectively eliminating self radiation from the obtained signal (cp. Sec. 2.3). Taken together, the MASCOT radiometer MARA has been shown to be capable of measuring surface brightness temperatures with an uncertainty of better than 1 K using its most sensitive SiLP channel, whereas the bandpass channels will allow for a determination of surface brightness temperatures in the 5.5-15.5 µm range if measurements are taken above 273 K.

4 Summary and Conclusions

The Hayabusa 2 spacecraft has been launched on the 3rd of December 2014 and is currently on its way to rendezvous with the C-type asteroid 1999 JU3 in spring 2018. Hayabusa 2 carries the MASCOT lander, which will be deployed in late 2018 to investigate the target asteroid in-situ (Lange et al. 2012). One of the MASCOT payloads is the MARA instrument, which will measure the asteroid's surface brightness temperature, from which the asteroid's thermal inertia will be derived. In addition, MARA will characterize the spectral slope of the surface in the 5.5 to 15.5 µm wavelength range, thus supporting the spectral characterization obtained by the orbiter near infrared spectrometer (Kitazato et al. 2015).

MARA has been developed starting from heritage design of the MUPUS-TM (Spohn et al. 2007) and MERTIS radiometers (Hiesinger et al. 2010), and has been build, qualified, and calibrated at the Institute of Planetary Research of the German Aerospace Center (DLR). The instrument consists of three functional subunits, comprising the

sensor head, backend electronics, as well as an on-board calibration target. Together, these element weight 313 g, and the instrument's power uptake is 0.31 W. In addition, heating power between 0 and 2 W is required to equilibrate the instruments sensor head to one of its three operating setpoints.

The instrument has been radiometrically calibrated between 123 and 373 K, and the resulting temperature uncertainty is 1 K in the most sensitive channel. Noise is dominated by thermal noise, and the Noise Equivalent Temperature Difference (NETD) is 0.1 K at 123 K target temperature. Measurements are repeatable to within 1 K, and this uncertainty includes contributions from unknown thermal gradients across the instrument itself. A second channel dedicated to surface brightness temperature determination uses the same wavelength range as the orbiter thermal mapper (Okada et al. 2015) and has similar performance characteristics (1.5 K temperature uncertainty, 0.1 K NETD). Bandpass channels dedicated to the spectral characterization of the asteroid's surface have lower signal to noise, but yield similar performance as long as the target temperature is above 273 K. The error budget is dominated by contributions from the non-perfect homogenization of temperature across the sensor head, which is largely but not perfectly accounted for during calibration. Thermal and electronics noise are minor contributors to the total temperature uncertainty.

References

M. Abe, K. Kawakami, S. Hasegawa, D. Kuroda,, M. Yoshikawa, T. Kasuga, K. Kitazato, Y. Sarugaku, D. Kinoshita, S. Miyasaka, S. Urakawa, S. Okumura, Y. Takagi, N. Takato, T. Fujiyoshi, H. Terada, T. Wada, Y. Ita, F. Vilas, P. R. Weissman, Y.-J. Choi, S. Larson, S. J. Bus, A. Tokunaga, T. G. Müller, Ground-based observational campaign for Asteroid 162173 1999 JU3, 39th Lunar and Planetary Science Conference, abstract 1594 (2008).

G.E. Arnold, J. Helbert, H. Hiesinger, H. Hirsch, E. Jessberger et al., Mercury radiometer and thermal infrared spectrometer–a novel thermal imaging spectrometer for the exploration of Mercury, *J. Appl. Remote Sens.*, 2(1), 023528 (2008).

O.S. Barnouin-Jha, A.F. Cheng, T. Mukai, S. Abe, N. Hirata, R. Nakamura, R.W. Gaskell, J. Saito, B.E. Clark, Small-scale topography of 25143 Itokawa from the Hayabusa laser altimeter, *Icarus*, 198, 1, 108-124 (2008).

J.P. Bibring et al., *Space Sci. Rev.*, this issue (2015).

J. Biele, S. Ulamec, Capabilities of Philae, the Rosetta Lander, in: Origin and Early Evolution of Comet Nuclei, Space Sciences Series of ISSI, 28, 275-289 (2008).

R.P. Binzel, A.W. Harris, S.J. Bus, T.H. Burbine, Spectral Properties of Near-Earth Objects: Palomar and IRTF Results for 48 Objects Including Spacecraft Targets (9969) Braille and (10302) 1989 ML, *Icarus* 151, 139-149 (2001).

W.F. Bottke, D. Vokrouhlický, D.P. Rubincam, D. Nesvorný, The Yarkovsky and YORP Effects: Implications for Asteroid Dynamics, *Ann. Rev. Earth Plan. Sci.*, 34: 157-191 (2006).

S.J. Bus, R.P. Binzel, Phase II of the Small Main-Belt Asteroid Spectroscopic Survey. A Feature-Based Taxonomy, *Icarus* 158, 1, 146-177 (2002).

H. Campins, J.P. Emery, M. Kelley, Y. Fernández, J. Licandro, M. Delbó, A. Barucci, E. Dotto, Spitzer observations of spacecraft target 162173 (1999 JU3), *A&A*, 503, L17-L20 (2009).

S.R. Chesley, S.J. Ostro, D. Vokrouhlický, D. Čapek, J.D. Giorgini, M.C. Nolan, J.-L. Margot, A.A. Hine, L.A.M. Bennerd, A.B. Chamberlin, Direct Detection of the Yarkovsky Effect by Radar Ranging to Asteroid 6489 Golevka, *Science*, 302 (5651), 1739-1742 (2003).

B.J.R. Davidsson, H. Rickman, J.L. Bandfield, O. Groussin, P.J. Gutiérrez, M. Wilska, M.T. Capria, J.P. Emery, J. Helbert, L. Jorda, A. Maturilli, T.G. Müller, Interpretation of thermal emission. I. The effect of roughness for spatially resolved atmosphereless bodies, *Icarus*, 252, 1-21 (2015).

M. Delbo, Thermal inertia of near-Earth asteroids and implications for the magnitude of the Yarkovsky effect, *Icarus*, 190, 236-249 (2007).

P. Farinella, D. Vokrouhlický, W.K. Hartmann, Meteorite Delivery via Yarkovsky Orbital Drift, *Icarus*, 140, 369-378 (1998).

J. Gómez-Elvira, C. Armiens, L. Castañer, M. Domínguez, M. Genzer, F. Gómez, R. Haberle, A.-M. Harri, V. Jiménez, H. Kahanpää, L. Kowalski, A. Lepinette, J. Martín, J. Martínez-Frías, I. McEwan, L. Mora, J. Moreno, S. Navarro, M.A. de Pablo, V. Peinado, A. Peña, J. Polkko, M. Ramos, N.O. Renno, J. Ricart, M. Richardson, J. Rodríguez-Manfredi, J. Romeral, F.E. Sebastián, J. Serrano, M. de la Torre Juárez, J. Torres, F. Torrero, R. Urquí, L. Vázquez, T. Velasco, J. Verdasca, M.-P. Zorzano, J. Martín-Torres, REMS: The Environmental Sensor Suite for the Mars Science Laboratory Rover, *Sp. Sci. Rev.*, 170, 1-4, 583-640 (2012).

M. Grott, J. Knollenberg, A. Maturilli, J. Helbert, N. Müller, E. Kührt, Mineralogical Surface Characterization Using the MASCOT Radiometer MARA on the Hayabusa 2 Mission, 44th Lunar and Planetary Science Conference, abstract 1597 (2013).

S. Hasegawa, T.G. Müller, K. Kawakami, T. Kasuga, T. Wada, Y. Ita, N. Takato, H. Terada, T. Fujiyoshi, M. Abe, Albedo, Size, and Surface Characteristics of Hayabusa-2 Sample-Return Target 162173 1999 JU3 from AKARI and Subaru Observations, *PASP*, 60, 399 - 405 (2008).

D. Hercik, H.-U. Auster, J. Blum, K.-H. Fornacon, M. Fujimoto, K. Gebauer, C. Guttler, O. Hillenmaier, A. Hördt, I. Richter, B. Stoll, B. Weiss, K.-H. Glaßmeier, MasMag: The MASCOT Magnetometer experiment, *Space Sci. Rev.*, this issue (2015)

H. Hiesinger, J. Helbert, MERTIS Co-I Team, The Mercury Radiometer and Thermal Infrared Spectrometer (MERTIS) for the BepiColombo mission, *Plan. Space Sci.*, 58, 1-2, 144-165 (2010)

T.-M. Ho, V. Baturkin, R. Findlay, C. Grimm, J.T. Grundmann, C. Hobbie, E. Ksenik, C. Lange, K. Sasaki, M. Schlotterer, M. Talapina, N. Termtanasombat, L. Witte, M. Wrasmann, G. Wübbels, J. Rößler, C. Ziach, J. Biele, C. Krause, S. Ulamec, M. Lange, O. Mierheim, R. Lichtenheldt, M. Meier, J. Reill, H.J. Sedlmayr, P. Bousquet, A. Bellion, O. Bompis, C. Cenac-Morthe, M. Deleuze, S. Fredon, E. Jurado, E. Canalias, R. Jaumann, J.-P. Bibring, M. Grott, H. U. Glassmeier, L. Celotti, F. Cordero, J. Hendrikse, MASCOT - The Mobile Asteroid Surface Scout onboard the Hayabusa2 Mission, *Space Sci. Rev.*, this issue (2015).

M. Ishiguro, D. Kuroda, S. Hasegawa, M.-J. Kim, Y.-J. Choi, N. Moskovitz, S. Abe, K.-S. Pan, J. Takahashi, Y. Takagi, A. Arai, N. Tokimasa, H.H. Hsieh, J.E. Thomas-Osip, D.J. Osip, M. Abe, M. Yoshikawa, S. Urakawa, H. Hanayama, T. Sekiguchi, K. Wada, T. Sumi, P.J. Tristram, K. Furusawa, F. Abe, A. Fukui, T. Nagayama, D.S. Warjurkar, A. Rau, J. Greiner, P. Schady, F. Knust, F. Usui, T.G. Müller, Optical Properties of (162173) 1999 JU3: In Preparation for the JAXA Hayabusa 2 Sample Return Mission, *ApJ*, 792, 1, 74 (2014).

B.M. Jakosky, On the thermal properties of Martian fines, *Icarus*, 66, 117-124 (1986).

R. Jaumann, N. Schmitz, A. Koncz, H. Michaelis, S. Schroeder, S. Mottola, F. Trauthan, H. Hoffmann, T. Roatsch ,D. Jobs, J. Kachlicki, B. Pforte, R. Terzer, M. Tschentscher, S. Weisse, U. Mueller, T.-M. Ho, M. Grott, J.P. Bibring, J. Biele, S. Ulamec, B. Broll, A. Kruselburger, L. Perez-Prieto, The camera of the MASCOT asteroid lander on board Hayabusa-2, *Space Sci. Rev.*, this issue (2015).

E. Kessler, *Proc. of Sensor 2005, 12th International Conference*, Vol. I, Nürnberg, 73-78 (2005).

K. Kitazato, T. Iwata, *Space Sci. Rev.*, this issue (2015).

C. Lange et al., *Europ. Conf. on Spacecraft Struct., Materials and Environmental Testing*, 20.-23.Mrch 2012, Noordwijk, Netherlands (2012).

D. Lazzaro, M.A. Barucci, D. Perna, F.L. Jasmim, M. Yoshikawa, J.M.F. Carvano, Rotational spectra of (162173) 1999 JU3, the target of the Hayabusa2 mission, *A&A*, 549, L2 (2013).

A. Maturilli et al., *EPSC Abstracts*, Vol. 7, EPSC2012-487 (2012).

M.T. Mellon, B.M Jakosky, H.H. Kieffer, P.R. Christensen, High-Resolution Thermal Inertia Mapping from the Mars Global Surveyor Thermal Emission Spectrometer, *Icarus*, 148, 437-455 (2000).

P. Michel, M. Delbo, Orbital and thermal evolutions of four potential targets for a sample return space mission to a primitive near-Earth asteroid, *Icarus*, 209,2,520-534 (2010).

T. G. Müller, J. Durech, S. Hasegawa, M. Abe, K. Kawakami, T. Kasuga, D. Kinoshita, D. Kuroda, S. Urakawa, S. Okumura, Y. Sarugaku, S. Miyasaka, Y. Takagi, P. R. Weissman, Y.-J. Choi, S. Larson, K. Yanagisawa, S. Nagayama, Thermo-physical properties of 162173 (1999 JU3), a potential flyby and rendezvous target for interplanetary missions , *A&A*, 525, A145 (2011).

T. Okada et al., *43rd LPSC*, The Woodlands, abstract 1498 (2012).
T. Okada et al., *Space Sci. Rev.*, this issue (2015).
S.J. Paddack, Rotational bursting of small celestial bodies: Effects of radiation pressure, *J. Geophys. Res.*, 74, 4379-4381 (1969).
N.E. Putzig, M.T. Mellon, K.A. Kretke, R.E. Arvidson, Global thermal inertia and surface properties of Mars from the MGS mapping mission, *Icarus*, 173, 325-341 (2005).
D.P. Rubincam, Asteroid orbit evolution due to thermal drag, *J.Geophys.Res.*, 100, E1, 1585-1594 (1995).
V.I. Sapritsky et al., *Temperature: Its Measurement and Control in Science and Industry*, vol. 7, 619-624 (2003).
J.R. Spencer, L.A Lebofsky, M.V Sykes, Systematic biases in radiometric diameter determinations, *Icarus* 78, 337-354 (1989).
T. Spohn, K. Seiferlin, A. Hagermann, J. Knollenberg, A.J. Ball, M. Banaszkiewicz, J. Benkhoff, S. Gadomski, W. Gregorczyk, J. Grygorczuk, M. Hlond, G. Kargl, E. Kührt, N. Kömle, J. Krasowski, W. Marczewski, J.C. Zarnecki, Mupus - A Thermal and Mechanical Properties Probe for the Rosetta Lander Philae, *Sp. Sci. Rev.*, 128, 1-4, 339-362 (2007).
T. Spohn, J. Knollenberg, A. J. Ball, M. Banaszkiewicz, J. Benkhoff, M. Grott, J. Grygorczuk, C. Hüttig, A. Hagermann, G. Kargl, E. Kaufmann, N. Kömle, E. Kührt, K. J. Kossacki, W. Marczewski, I. Pelivan, R. Schrödter, K. Seiferlin, Thermal and mechanical properties of the near-surface layers of comet 67P/Churyumov-Gerasimenko, *Science*, 349 (6247) (2015)
J. Takita, H. Senshu, S. Tanaka, this issue.
J. Veverka, P. Thomas, A. Harch, B. Clark, J.F. Bell III, B. Carcich, J. Joseph, S. Murchie, N. Izenberg, C. Chapman, W. Merline, M. Malin, L. McFadden, M. Robinson, Encounter with Asteroid 253 Mathilde: Overview, *Icarus*, 140, 1, 3 - 16 (1999).
F. Vilas, Spectral Characteristics of Hayabusa 2 Near-Earth Asteroid Targets 162173 1999 JU3 and 2001 QC34,*Astron. J.*, 153, 1101-1105 (2008).